

## Journal Name

Crossmark

PAPER

RECEIVED

dd Month yyyy

REVISED

dd Month yyyy

## Density Limit Experiments and Core-localized Kinetic MHD Activities in HL-2A Ohmic Heating Plasmas

L. W. Hu<sup>1</sup>, W. Chen<sup>1\*</sup>, P. W. Shi<sup>1</sup>, T. Long<sup>1</sup>, J. Q. Xu<sup>1</sup>, R. R. Ma<sup>1</sup>, Y. G. Li<sup>1</sup>, L. M. Yu<sup>1</sup>, X. Yu<sup>1</sup>, M. Jiang<sup>1</sup>, T. F. Sun<sup>1</sup>, J.M. Gao<sup>1</sup>, Y. B. Dong<sup>1</sup>, X. L. Zhu<sup>1</sup>, Z. B. Shi<sup>1</sup><sup>1</sup>Joint Laboratory for Fusion Product and Energetic Particle, Southwestern Institute of Physics, P.O. Box 432 Chengdu 610041, China

\*W. Chen

E-mail: chenw@swip.ac.cn

Keywords: Density limit, MHD instability, Alfvénic ion temperature gradient mode, Disruption

## Abstract

The density limit is a mysterious barrier to magnetic confinement nuclear fusion, and is still an unresolved issue. In this paper, we will present the experimental results of the density limit and core-localized kinetic MHD instabilities on HL-2A. Firstly, the high density shots with  $ne/ne_G > 1$  have been achieved by the conventional gas-puff fuelling method in Ohmic heating plasmas, and the corresponding duration time is close to  $t \sim 500$  ms ( $\sim 30\tau_E$ ), where  $\tau_E$  is the global energy confinement time. Secondly, it is found for the first time that there are kinetic MHD instabilities in the core plasmas while  $ne/ne_G \sim 1$ . The analysis suggests that the core-localized MHD activities belong to Alfvénic ion temperature gradient (AITG) modes or kinetic ballooning modes (KBM), and firstly it is found on experiment that they trigger the minor or major disruption of bulk plasmas while the density profile is peaked. These new findings are of great importance to figure out and understand the origin of the density limit.

## 1 Introduction

High plasma density ( $ne$ ) is essential for accessing high fusion gain since the fusion power density ( $P$ ) scales as  $P \propto ne^2$ . However, there is a limit (known as Greenwald limit) for tokamak high density shots[1, 2]. The Greenwald limit is an empirical limit for the achievable line-averaged plasma density on experiments, namely  $ne_G = I_p/\pi a^2$ , where  $ne_G$  is the line-averaged plasma density in units of  $10^{20} m^{-3}$ ,  $I_p$  the plasma current in MA and  $a$  the minor radius in m. Generally, when the Greenwald density is reached, the bulk plasma frequently disrupts as well as the shot halts. Therefore, the density limit represents an operational limit for tokamaks. It is crucial to realize the steady-state high density operation. For the ITER baseline scenario, the density of H-mode plasmas is up to  $0.85ne_G$ [3]. Many experimental results indicate that the density limit occurrence is correlated to the plasma edge cooling[4], multifaceted asymmetric radiation from edge (MARFE)[5], current channel shrinkage, macroscopic magnetohydrodynamics (MHD) activities (mainly tearing modes)[6, 7, 8, 9], edge turbulence[10, 11], and so forth. These results indicate that the density limit originates from the plasma edge region. Meanwhile, some experimental results also suggest the density limit can be exceeded by the plasma core fuelling[12], edge pumping, or modification of particle transport, which leads to peaked density profiles[13]. The physical mechanisms governing the density limit of plasmas are not yet fully understood because they involve a complex array of interrelated phenomena.

Prior to the onset of density limit disruptions, tearing mode instabilities often emerge frequently. The prevailing explanation attributes this phenomenon to an increased current gradient caused by current quenching following edge cooling[14]. However, in the absence of tearing modes, this account still fails to clarify the underlying reason for the restriction on core density rise. The transition from linear Ohmic confinement (LOC) to saturated Ohmic confinement (SOC) in Ohmic heated plasmas [15] suggests that as the plasma approaches the density limit, certain mechanisms degrade its energy confinement. A plausible explanation for this degradation involves micro-turbulence or various instabilities. Notably, the Alfvénic ion temperature gradient (AITG) mode has been identified during the SOC phase in Ohmic heated plasmas on the HL-2A tokamak [16]. Such instabilities may be linked to the deterioration of plasma confinement. Experimentally, AITG can also be referred to as kinetic ballooning modes (KBM). Simulations using various numerical codes indicate that the excitation of

the KBM/AITG mode depends on a specific  $\beta$  (pressure ratio) threshold and becomes more unstable under weak magnetic shear conditions [17, 18, 19]. Besides the KBM/AITG mode, other instabilities such as the ion temperature gradient (ITG) mode [20] and the micro-tearing mode (MTM) [21] may also exist in the plasma core. MTM is primarily destabilized by the electron temperature gradient, while the ITG mode is mainly driven by the ion temperature gradient. Moreover, the ITG mode is stabilized in high-beta plasmas. In high-density plasmas produced by Ohmic heating, the parameter  $\beta$  exhibits an increase with rising density, and a substantial temperature gradient is not sustained. Thus, it is unlikely that either mode constitutes the primary cause of the observed density limit. In this paper, we provide a detailed description and analysis of experimental results on density limits and MHD activities obtained from the HL-2A tokamak.

The experiments reported here were conducted on the HL-2A tokamak [22] in lower single-null divertor deuterium plasmas, with a plasma current  $I_p \simeq 140 - 160$  kA and a toroidal magnetic field  $B_t \simeq 1.1 - 1.4$  T. The device has a major radius  $R_0 = 1.65$  m and a minor radius  $a = 0.4$  m, yielding an almost circular poloidal cross-section. The plasma-facing components are primarily made of graphite tiles. The line-averaged electron density is detected using a multi-channel HCOOH laser interferometry, and density profile is reconstructed via Abel inversion[23]. Density fluctuations were monitored non-locally using a two-channel microwave interferometry in the core region[24]. Electron temperature profiles were obtained from an optically thick, second-harmonic (X-mode) electron cyclotron emission (ECE) radiometer [25], while the central electron temperature was measured by Thomson scattering. Magnetic fluctuations were detected using toroidal and poloidal Mirnov coils[26]. To access high-density regimes, continuous gas puffing was employed, successfully producing peaked density profiles with  $ne/ne_G > 1$  where  $ne$  is the line-averaged electron density. The gas puff primarily raised the edge density, and through plasma self-organization, the entire density profile was elevated. The plasma density limit is known to occur across various types of heated plasmas. To minimize the influence of auxiliary heating methods—such as natural beam injection (NBI) and radio-frequency heating—this study focuses primarily on Ohmic heating plasmas in the HL-2A tokamak.

Section 2 presents the phenomenon of density perturbations in plasmas approaching the density limit, including broad-spectrum turbulence and core-localized magnetohydrodynamic (clMHD) instabilities. Section 3 introduces the experimental results from the HL-2A Ohmic heated plasmas, where gas-puffing is used to exceed the Greenwald density limit. Section 4 describes the conditions under which clMHD instabilities are easier to emerge. In section 5, clMHD modes are identified as KBM/AITGs and their impact on the plasma are analyzed. Finally, a summary in section 6.

## 2 Density perturbations in plasma close to density limit

Figure 1 shows two Ohmic-heated shots in HL-2A tokamak. Shot #38261 reaches a relative density of  $ne/ne_G \sim 1.07$  before disruption, while shot #38262 attains  $ne/ne_G \sim 0.99$ , as marked by the black arrows in Figure 1(b1,b2). The high density is achieved by conventional gas-puff fueling. As shown in Figure 1(a1,a2), the plasma current remains nearly constant during the density ramp-up phase. The total radiation power of plasma  $P_{rad}$  increases slightly as the plasma approaches the Greenwald density limit, suggesting that the disruption may not be caused by a radiative collapse. The magenta curves in Figure 1(b1,b2) indicate that the oxygen impurity levels  $I_{OVI}$  rises slightly with increasing density, consistent with  $P_{rad}$ . As indicated by the white arrows in Figure 1(c1,c2), the spectral range of density perturbations observed via microwave interferometry broadens with increasing density, evolving to a maximum frequency of approximately 200 kHz near the density limit. These perturbations are generally considered to be caused by turbulence, as turbulence-induced perturbations typically manifest as broad-spectrum disturbances in the frequency domain. This paper does not delve into the specific types of broad-spectrum turbulence discussed here, and as will be evident from Figure 5 later, these broad-spectrum turbulences are not always present in Ohmic heating density limit plasmas. Figure 1(d1, d2) shows the magnified views of the spectra corresponding to the black rectangular areas in Figure 1(c1, c2). The black arrows in Figure 1(d1) denote the onset time of the clMHD instabilities. The dashed elliptical line in Figure 1(d2) indicates the signature of the clMHD modes in the microwave interferometry spectrum. The term ‘clMHD’ is used for the modes observed in Figure 1(d1, d2) for the following reasons: 1. These modes are detectable in the microwave interferometry spectrum but not in the magnetic probe spectrum, indicating that they are localized in the plasma core. 2. Unlike turbulence, these modes exhibit coherent structures characteristic of MHD behavior. It is evident that clMHD modes are present in both shots; however, they exhibit higher intensity in shot #38262. Since both shots eventually reach the density limit, these clMHD modes are likely not the direct cause of disruption. However, their presence seems to reduce the achievable density: the plasma reaches  $ne/ne_G \sim 1.07$  in the case of

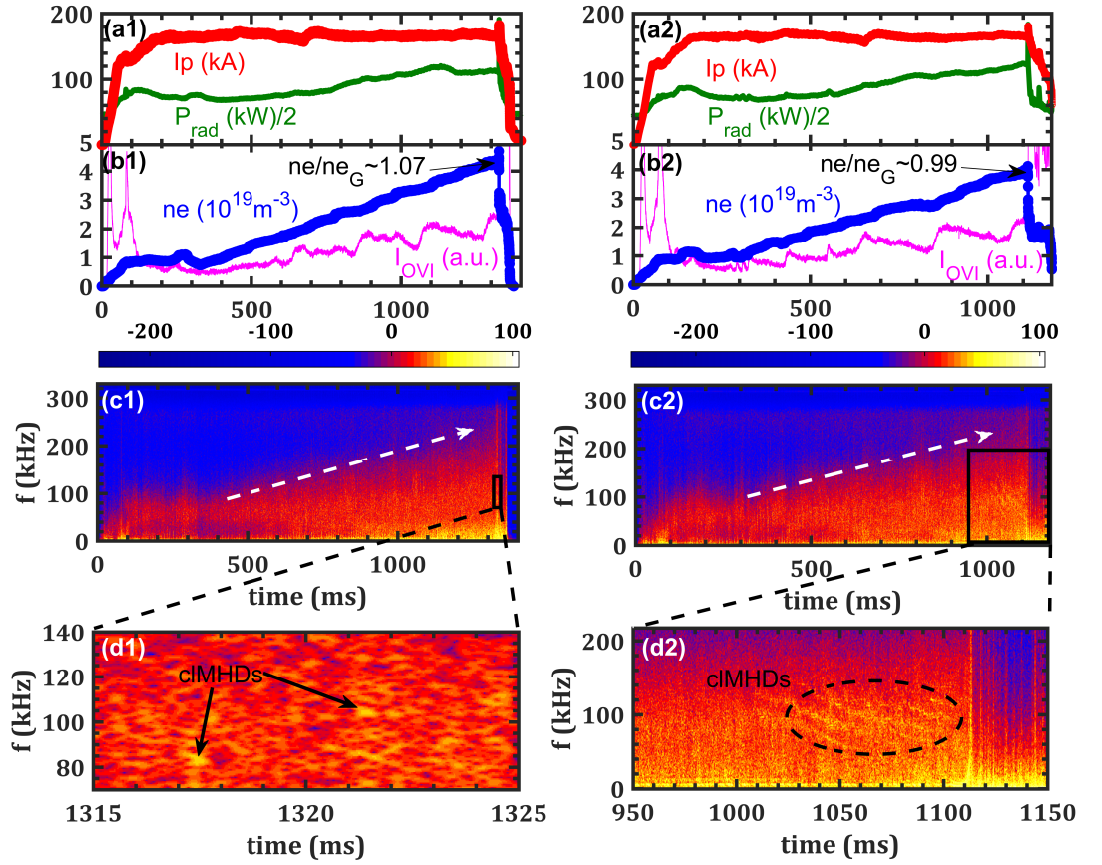


**Figure 1.** (a1) Time traces of plasma current  $I_p$  and total plasma radiation power  $P_{rad}$  for shot #38261. The red and green solid lines correspond to  $I_p$  and  $P_{rad}$ , respectively. (a2) Time traces of  $I_p$  and  $P_{rad}$  for shot #38262. (b1) Time traces of line-averaged plasma density  $ne$  and oxygen impurity spectral line  $I_{OVI}$  for shot #38261. The blue and magenta solid lines show  $ne$  and  $I_{OVI}$ , respectively. The black arrow marks the relative density level at the time of peak density. (b2) Time traces of  $ne$  and  $I_{OVI}$  for shot #38262. (c1) Spectrum of microwave interferometry signal for shot #38261, where the microwave interferometry channel passes through the center of the plasma. The white arrow indicates the trend of spectral broadening. (c2) Spectrum of the central microwave interferometry signal for shot #38262. (d1) Magnified view of spectrum as indicated by black rectangular in subfigure (c1). The black arrows indicate the onset time of clMHD modes. (d2) Magnified view of spectrum as indicated by black rectangular in subfigure (c2). The dashed elliptical line denotes signature of the clMHD modes.

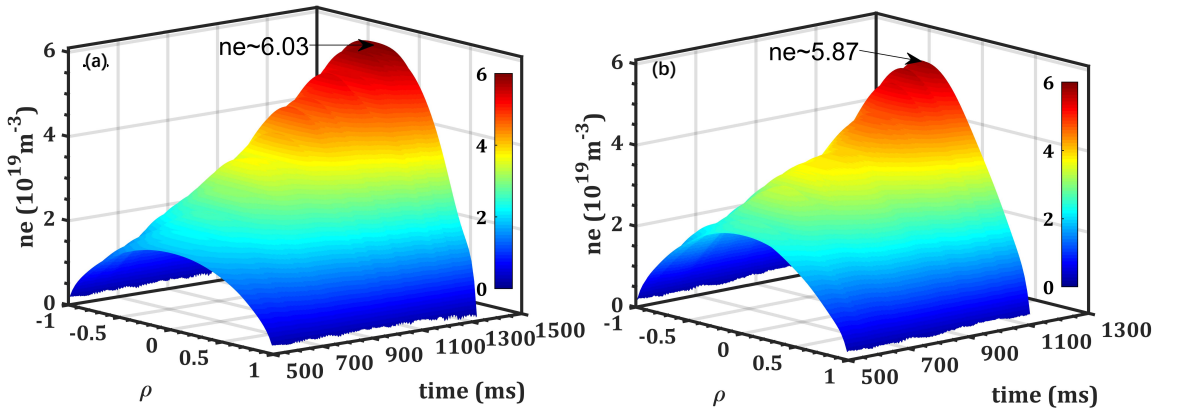


**Figure 2.** (a) Time evolution of the density profile for shot #38261, obtained from Abel inversion of laser interferometry data. The black arrow marks the core density before the density-limit disruption, with  $ne \sim 6.03 \times 10^{19} \text{ m}^{-3}$ . (b) Time evolution of the density profile for shot #38262. The core density prior to disruption is  $ne \sim 5.87 \times 10^{19} \text{ m}^{-3}$ . Here  $\rho = r/a$  is the normalized radius. The observed density ramp-up and peaking in both shots result from plasma self-organization under gas puffing.

weak instabilities, but only  $ne/ne_G \sim 0.99$  when the instabilities are stronger. This indicates that the clMHD modes lower the maximum attainable relative density.

According to Figure 1(d2), shot #38262 displays coherent instabilities in the frequency range of 50–150 kHz. The spectra correspond to the interferometry channel passing through the plasma center ( $z = 0$ ). Notably, these instabilities are absent in the horizontal interferometry channel located at  $z = 15$  cm (where  $z$  denotes the longitudinal direction of the device), indicating that the modes are localized within the region where  $r < 15$  cm, with  $r$  representing the minor radius. The frequency of a toroidal Alfvén eigenmode (TAE) is approximately given by  $f_{TAE} \sim v_A/(4\pi qR)$ , where  $q$  is the safety factor and  $v_A$  is the Alfvén velocity and  $R$  is the large radius[27]. At the  $q=1$  surface,  $f_{TAE}$  is approximately 210 kHz. The instability frequency observed in shot #38262 is about  $\frac{1}{2}f_{TAE}$ , suggesting a possible connection with shear Alfvén waves. As shown in Figure 1(d2), the frequency of the instabilities decreases as the plasma density increases. The observed frequency is influenced by the Doppler shift, and can be expressed as  $f_{lab} = f_{plasma} \pm n f_{v\phi}$ , where  $f_{lab}$  is the frequency in laboratory frame and  $f_{plasma}$  is frequency in plasma frame,  $n$  is the toroidal mode number and  $f_{v\phi}$  is the toroidal rotation frequency[28]. According to Figure 1(a2,b2) the plasma parameters in shot #38262 do not change significantly between 1000 ms and 1100 ms. Thus, the decrease in instability frequency may be attributed to a reduction in the toroidal mode number. These instabilities emerge tens of milliseconds before the density-limit disruption and may be partly linked to the onset of the disruption.

To clarify why instabilities are weaker in shot #38261 but stronger in #38262, we analyze in detail the evolution of the density profiles in both shots. Figure 2 shows the time-dependent density profiles for shots #38261 and #38262. Both shots exhibit clear density peaking. The peak electron density in shot #38261 reaches about  $\sim 6.03 \times 10^{19} \text{ m}^{-3}$ , while in shot #38262 it is approximately  $5.87 \times 10^{19} \text{ m}^{-3}$ . Moreover, the density peaking phenomenon is more pronounced in shot #38262 than in shot #38261. A more peaked density profile implies a stronger density gradient. Since both shots are Ohmically heated, a large temperature gradient is unlikely to develop. Therefore, the instabilities observed in shot #38262 are likely driven by the density gradient of thermal particles. These instabilities may exhibit a threshold in density gradient beyond which they become unstable. Under the present Ohmic heating and gas-puffing conditions, density peaking reflects a self-organizing behavior of the plasma.

### 3 Exceeding Greenwald density limit by gas-puffing on HL-2A

Through gas puffing, a high-density operational regime has been achieved on the HL-2A tokamak, in which the plasma density exceeds the Greenwald density limit. Figure 3 shows the time traces of plasma parameters for shots #38522 and #38581. In shot #38522, about 0.5 MW of NBI power is applied from 800 ms to 1250 ms; during other periods, both shots are sustained by Ohmic heating alone. The plasma current is  $I_p \sim 150$  kA in both shots. And the corresponding Greenwald density limit  $ne_G$  is about  $3.0 \times 10^{19} \text{ m}^{-3}$ . Both shots reach a maximum line-averaged electron density of approximately  $5.0 \times 10^{19} \text{ m}^{-3}$ . In shot #38581, the plasma current gradually decreases as density rises in the later stage, leading to a reduction in the Greenwald limit. For shot #38522, the maximum ratio of the electron density to the Greenwald density limit,  $ne/neG$ , is approximately 1.3, while for shot #38581, it is about 1.5. In both shots, the plasma remains above the Greenwald limit for more than 500 ms—roughly 30 times the energy confinement time  $\tau_E$ —indicating that the Greenwald limit does not constitute a strict barrier to plasma density. The ability to attain such high  $ne/neG$  values may be attributed to relatively low impurity content and comparatively weak plasma instabilities. As shown in the time traces of impurity signals ( $I_{OVI}$  and  $I_{CIII}$ ) and radiation power ( $P_{rad}$ ) in Figure 3, neither the overall radiation nor the impurity levels increase significantly before the density-limit disruption. During NBI heating in shot #38522, a slight rise in radiated power and oxygen impurity is observed, likely due to confinement degradation caused by the NBI. Tearing modes are detected in the magnetic signals of shot #38522 before 1300 ms, but they are weak until the density-limit disruption happens at about 2500 ms.

Shot #38581 experiences two minor disruptions, identified by a sudden increase in the amplitude of the poloidal magnetic perturbation signal,  $dB_\theta/dt$ . At the time of these minor disruptions, the plasma density is close to the Greenwald limit, with  $ne/neG \sim 1.0$ . In both discharges, the electron temperature decreases as density increases due to gas puffing. As a result, the plasma stored energy  $W_E$  does not rise significantly at high density, consistent with the scaling  $W_E \propto ne \cdot Te$ . The decrease in plasma temperature following density increase via fueling can be attributed to the following factors: 1. Direct cooling from the injection of low-temperature gas; 2. Increased radiation losses; As previously noted, the stored energy of the injected gas is negligible compared to that of the plasma. Thus, gas injection does not contribute to an increase in plasma stored energy, in accordance with energy conservation. Therefore, the nearly constant stored energy together with the gradually increasing density corresponds to a decreasing plasma temperature. This process describes the

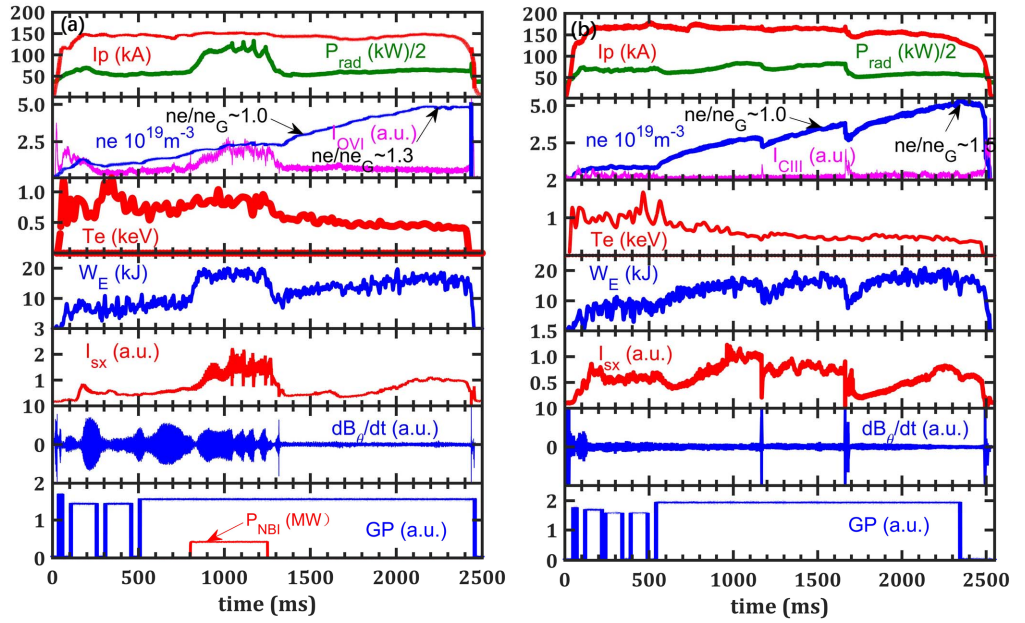


**Figure 3.** (a) Time traces of plasma parameters for shot #38522. (b) Time traces of plasma parameters for shot #38581. The following quantities are shown: plasma current  $I_p$  (red line); total radiation power of plasma  $P_{rad}$  (green line); line-averaged electron density  $ne$  (blue line); oxygen impurity level  $I_{OVI}$  (magenta line); carbon impurity level  $I_{CIII}$  (purple line); core electron temperature  $Te$  (red line); plasma stored energy  $W_E$  (blue line); soft X-ray (SXR) signal  $I_{SX}$  (red line); time-differential poloidal magnetic perturbation  $dB_\theta/dt$  (blue line); gas-puffing signal  $GP$  (blue line) and NBI power  $P_{NBI}$  (red line). Black arrows mark the times when the ratio  $ne/ne_G$  reaches 1.0 and its maximum value.

mechanism of direct cooling of the plasma by low-temperature gas. The radiation power of plasma scales as  $S_B \sim Z_{eff} n^2 T e^{1/2}$ , where  $Z_{eff}$  is the effective charge number[29]. Although impurity levels often rise at high density due to degraded confinement—leading to an increase in  $Z_{eff}$ —the radiated power shown in Figure 3 remains nearly constant. This indicates that increased radiation is not the primary cause of the temperature decrease in high-density plasmas.

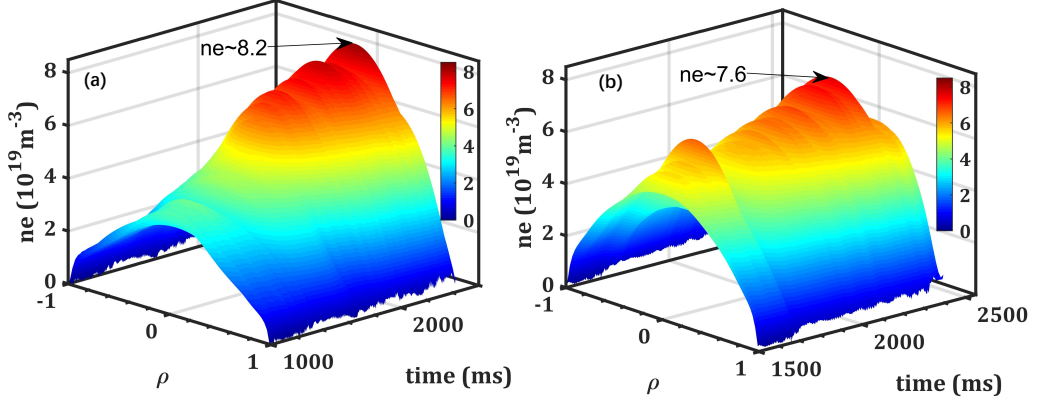


**Figure 4.** (a) Time evolution of the density profile for shot #38522, obtained from Abel inversion of laser interferometry data. The black arrow indicates the core density before the density-limit disruption,  $ne \sim 8.2 \times 10^{19} \text{ m}^{-3}$ . (b) Time evolution of the density profile for shot #38581. The core density prior to disruption is  $ne \sim 7.6 \times 10^{19} \text{ m}^{-3}$ . Here  $\rho = r/a$  denotes the normalized radius. The overall drop in plasma density after 1500 ms corresponds to a minor disruption occurring around 1660 ms.

Figure 5(a) shows the microwave interferometry spectrum for shot #38522. In this discharge, the electron density exceeds the Greenwald limit after 1900 ms. After 2100 ms, multiple instabilities appear in the spectrum, with frequencies ranging from near zero up to 150 kHz. By combining Figure 1(d2) and Figure 5(a), it can be seen that these clMHD modes do not necessarily occur at a specific  $ne/ne_G$  value (e.g.,  $ne/ne_G \sim 1$ ), but rather emerge tens of milliseconds before a density limit disruption. This experimental observation suggests that these clMHD modes may play a significant role in the density limit disruption process. For instance, in shot #38262, clMHD modes appear just before  $ne/ne_G$  reaches  $\sim 1.0$ , followed shortly by a density limit disruption. In contrast, in shot

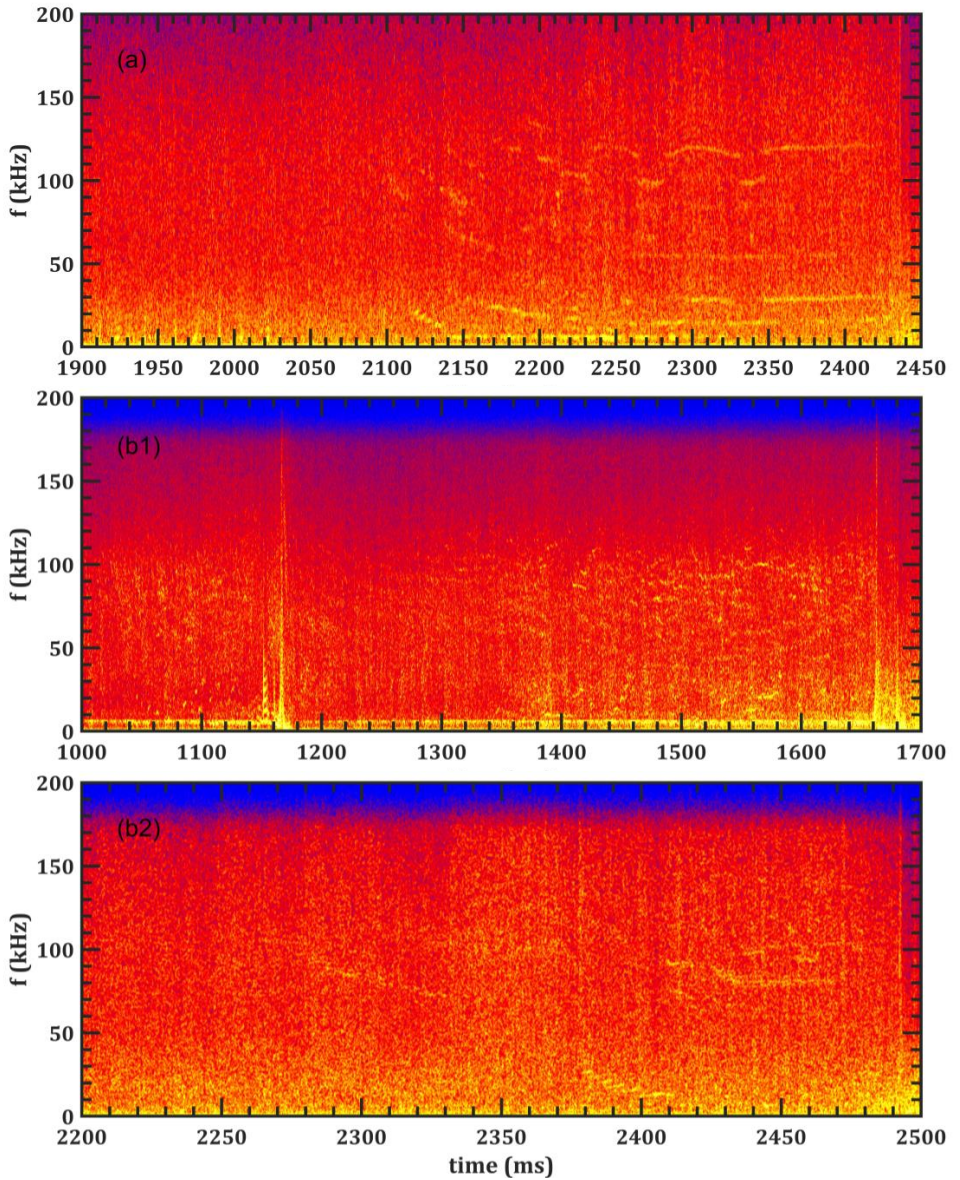


**Figure 5.** (a) Microwave interferometry spectrum before the density-limit disruption in shot #38522, showing instabilities in the 0–130 kHz range. (b1) Microwave interferometry spectrum before the minor disruption in shot #38581, with instabilities emerging in the 0–100 kHz range. (b2) Microwave interferometry spectrum before the major density-limit disruption in shot #38581.

#38522, although the plasma density has already exceeded the Greenwald density limit prior to 2100 ms, a disruption does not occur immediately. It is only after 2100 ms, with the continued density increase and further evolution of the clMHD modes, that the disruption ultimately takes place.

The TAE frequency at  $q=2$  surface is about 96 kHz during the time period depicted in Figure 5(a). Based on frequency, the clMHD modes in the spectrum are more consistent with instabilities such as KBM (also referred to as AITG) or beta-induced Alfvén eigenmode (BAE) [30, 31]. It should be noted that for the KBM/AITG, the frequency satisfies  $f_{KBM} \sim f_{BAE} < f_{TAE}$ . Moreover,  $f_{KBM} \sim f_{*pi} \sim f_{ti}$ , where  $f_{*pi}$  is the ion diamagnetic drift frequency and  $f_{ti}$  is the ion transit frequency [32]. The ratio  $f_{BAE}/f_{TAE}$  is given approximately by  $\sim 2q\sqrt{(7/4)\beta_i + \beta_e}$ . For shot #38522, using typical core values  $q \sim 2$  and  $\beta = \beta_i + \beta_e \sim 0.005$ , this ratio is about 0.47. Both experimental and theoretical studies suggest that KBM/AITG frequencies are generally lower than those of BAE, and their durations are shorter [33]. This is because KBM/AITG excitation is highly sensitive to the presence of rational surfaces, whereas BAE is less sensitive. The instabilities below 30 kHz, appearing as “Christmas lights” in the spectrum, are likely KBM/AITG modes. Since TAE excitation requires a particle energy threshold that is generally not met in Ohmic plasmas due to the lack of energetic particles [34], the TAE instabilities are not considered in this paper.

Figure 5(b1) shows the microwave interferometry spectrum for shot #38581 during the interval

1000–1700 ms. Two minor disruptions are observed in this shot, appearing in the spectrum as rapidly growing disturbances emerging from near zero frequency. Shortly before each minor disruption (at approximately 1160 ms and 1680 ms), multiple instabilities below 100 kHz also arise. The spectrum again shows instabilities that can be grouped into two frequency categories. The TAE frequency at  $q=2$  surface is about 120 kHz during the shown time period in figure 5(b1). The frequency of instabilities in figure 5(b1) is in the range of  $(0, f_{TAE})$ . Figure 5(b2) displays the spectrum from 2200 ms to 2500 ms for the same shot. Similar low-frequency “Christmas light”-like instabilities and high-frequency instabilities also appear prior to the major disruption.

As shown in Figure 1(b1,b2), the line-averaged plasma density in shots #38261 and #38262 rises continuously before density-limit disruptions occur. In contrast, for shot #38522 under continuous gas puffing (Figure 3(a)), the line-averaged density stops increasing once it reaches its maximum (corresponding to  $ne/neG \sim 1.3$ ). Two possible explanations can be considered for this behavior. One is that the high plasma density degrades the fueling efficiency of gas puffing, preventing further density increase. The other is that after the peak density is reached, some plasma-internal mechanism—such as specific instabilities—limits further density rise.

The first explanation is plausible because, as indicated in Figure 4, the peak core density in shot #38522 is about  $8.2 \times 10^{19} \text{ m}^{-3}$ , while in shot #38581 it is approximately  $7.6 \times 10^{19} \text{ m}^{-3}$ . Despite shot #38581 having a higher relative density  $ne/neG$  than shot #38522 (Figure 3), its core density is lower. This apparent contradiction stems from the gradual decrease in plasma current in shot #38581, which reduces its Greenwald limit  $neG$ , while the current in shot #38522 remains steady. Moreover, although shot #38581 reaches a higher line-averaged density, its core density is lower, implying a flatter density profile with a smaller overall gradient, as seen in Figure 4. This may explain why more instabilities are observed in the microwave interferometry spectrum of shot #38522 than in that of shot #38581 (Figure 5(a, b2)).

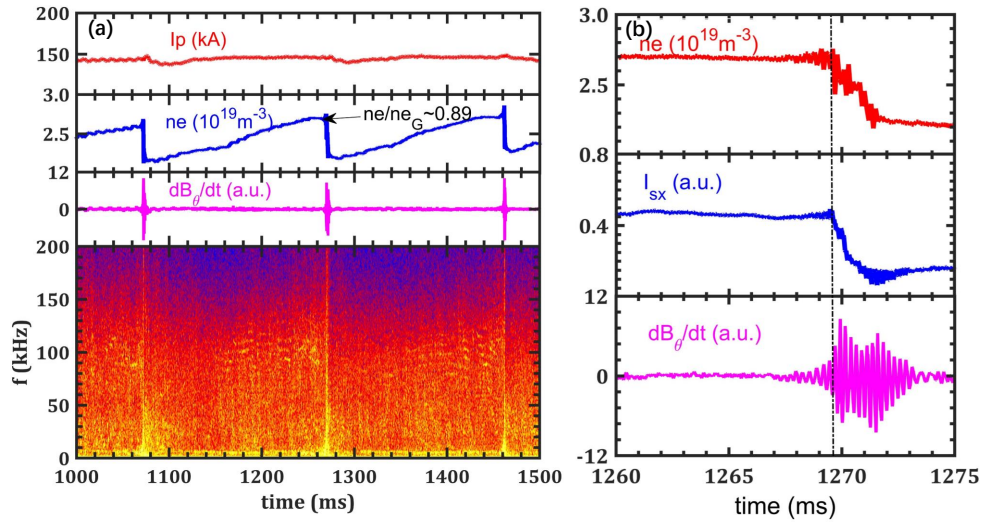
The second explanation also remains viable. According to Figure 3(a), the line-averaged density in shot #38522 stops increasing after about 2100 ms, even though gas puffing continues until approximately 2450 ms. Coincidentally, a variety of instabilities emerge in the core region starting around 2100 ms (Figure 5(a)), suggesting that these instabilities could indeed be responsible for limiting further density increase.

#### 4 Scenario analysis for the onset of clMHD modes

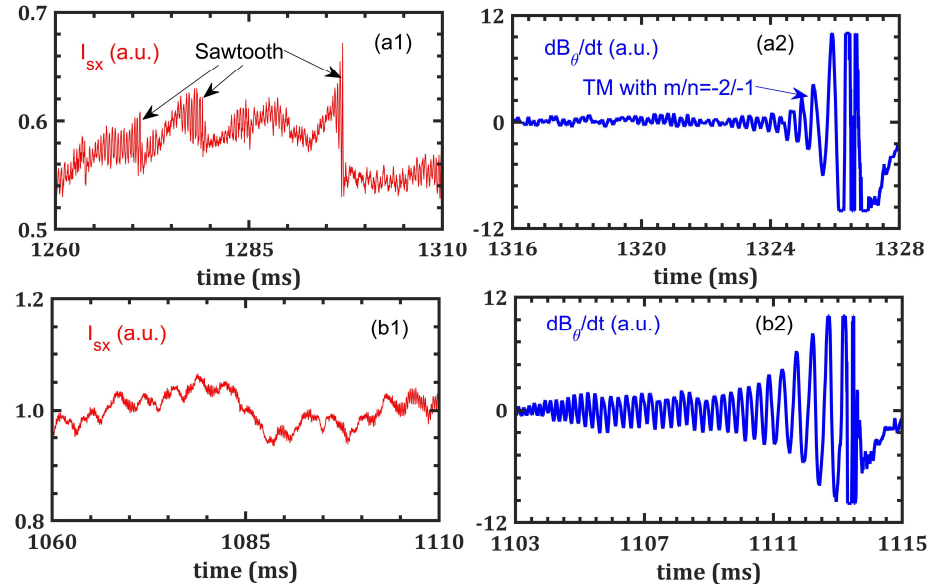
Figure 6 shows the time traces of plasma parameters and the microwave interferometry spectrum for shot #38570. In this discharge, three minor disruptions occur between 1000 ms and 1500 ms. Minor disruptions are identified by small upward spikes in the plasma current, accompanied by a rapid drop in plasma density or a sharp rise in magnetic perturbations. Since the maximum Greenwald fraction reaches  $ne/neG \sim 0.89$ , the minor disruptions are attributed to the density limit. In the tens of milliseconds preceding each minor disruption, instabilities in the frequency range of about 70–120 kHz repeatedly appear in the microwave interferometry spectrum. Zoomed-in views of the plasma parameters are provided in Figure 6(b). The vertical dashed line marks the time of a minor disruption. Following the occurrence of a minor disruption, the SXR level and magnetic perturbation begin to increase. Notably, the density perturbations already rise before the disruption, indicating that they act as precursors to the minor density-limit disruptions. As shown in Figures 5 and 6, when the plasma density approaches the density limit, the coincidental occurrence of clMHD modes makes the plasma more likely to experience either a major or minor disruption. Corresponding to the recurrent instances of clMHD modes and minor disruptions near the density limit in Figure 6(a), the physical process can be interpreted as a cyclic sequence: the density increases toward the Greenwald limit, triggering the onset of clMHD modes, which leads to a minor disruption. This event causes the density to decrease, resulting in the cessation of clMHD modes, after which the density begins to rise again. The repeated occurrence of such clMHD modes in a single discharge implies that their appearance is facilitated by a higher plasma density or a more peaked density profile.

Figure 7(a1) shows the raw SXR signal for shot #38261, with sawtooth oscillations visible between 1260 ms and 1310 ms. This indicates that the safety factor in the plasma core is less than unity ( $q < 1$ ), hence the presence of a  $q = 1$  surface. Figure 7(a2) presents the raw time derivative of the poloidal magnetic perturbation,  $dB_\theta/dt$ , for the same shot. A tearing mode (TM) with mode numbers  $m/n = 2/-1$  appears after 1324 ms, ultimately leading to a density-limit disruption. Figure 7(b1) displays the raw SXR signal for shot #38262. Here, the SXR intensity begins to decrease around 1080 ms, and no sawtooth activity is observed. Figure 7(b2) shows the corresponding  $dB_\theta/dt$  signal for shot #38262, where a TM also causes the disruption. Compared to shot #38261, however, the  $dB_\theta/dt$  signal in shot #38262 exhibits a larger amplitude even before the TM emerges.

As seen in Figure 1, clMHD modes are present in the density perturbation spectrum prior to



**Figure 6.** (a) Time traces of plasma parameters and microwave interferometry spectrum for shot #38570. Black arrows mark the ratio  $ne/neG$  prior to each density-limit minor disruption. Instabilities are observed in the interferometry spectrum before all three minor disruptions shown. (b) Zoomed-in view of plasma parameters for the same shot. The vertical dashed line indicates the time of a minor disruption. Displayed traces include: plasma current  $I_p$  (red), electron density  $ne$  (blue), time-differential poloidal magnetic perturbation  $dB_\theta/dt$  (magenta) and soft X-ray level  $I_{SX}$  (blue).



**Figure 7.** (a1) Raw SXR signal  $I_{SX}$  (red) for shot #38261. The black arrows indicate the moments of sawtooth crashes. (a2) Raw signal of time-differential poloidal magnetic perturbation  $dB_\theta/dt$  (blue) for shot #38261. The blue arrow indicates the occurrence of a tearing mode (TM) with mode numbers  $m/n=-2/-1$ . (b1) Raw SXR signal  $I_{SX}$  (red) for shot #38262. (b2) Raw signal of time-differential poloidal magnetic perturbation  $dB_\theta/dt$  (blue) for shot #38262.

the disruption. However, in shot #38261, the clMHD modes are weaker in intensity and fewer in number, corresponding to the scenario shown in Figure 7(a1, a2). In shot #38262, the clMHD modes exhibited greater intensity and more in number, aligning with the case depicted in Figure 7(b1, b2). Thus, clMHD modes are more likely to be excited when the core safety factor  $q_0$  exceeds 1.

In a single shot, a similar phenomenon is observed before and after the appearance of clMHD modes. Figures 8(a1) and (a2) present the raw SXR signals obtained during shot #38522 show the raw SXR signals from shot #38522 during two different time intervals: one without clMHD modes in the microwave interferometry spectrum (a1), and the other with clMHD modes present (a2). The appearance of sawtooth oscillations in (a1) indicates the existence of a rational surface with safety factor  $q=1$  at that time. In this interval, the SXR intensity  $I_{SX}$  rises over time, consistent with the increasing plasma density. In contrast, Figure 8(a2) shows a gradual decline in  $I_{SX}$  over time,

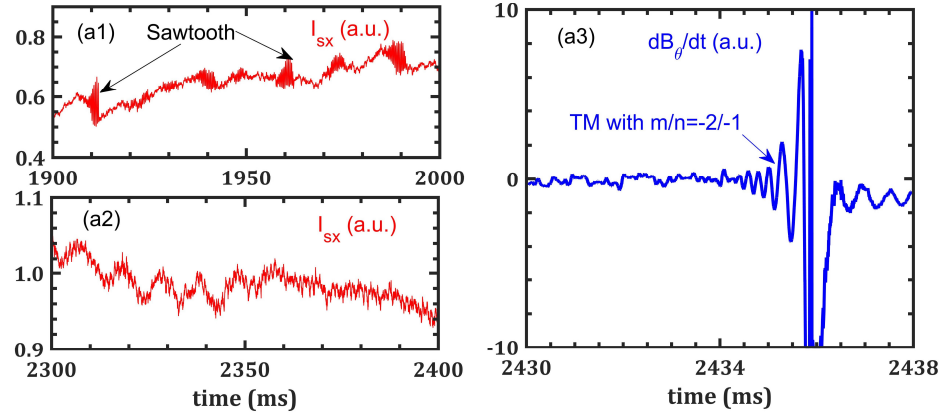


**Figure 8.** (a1) Raw SXR signal  $I_{SX}$  for shot #38522. Black arrows mark sawtooth crashes. (a2) Raw signal of SXR level  $I_{SX}$  for shot #38522. (a3) Raw time derivative of poloidal magnetic perturbation  $dB_\theta/dt$  for shot #38522. Blue arrow indicates the occurrence of a TM with mode numbers  $m/n=-2/-1$ .

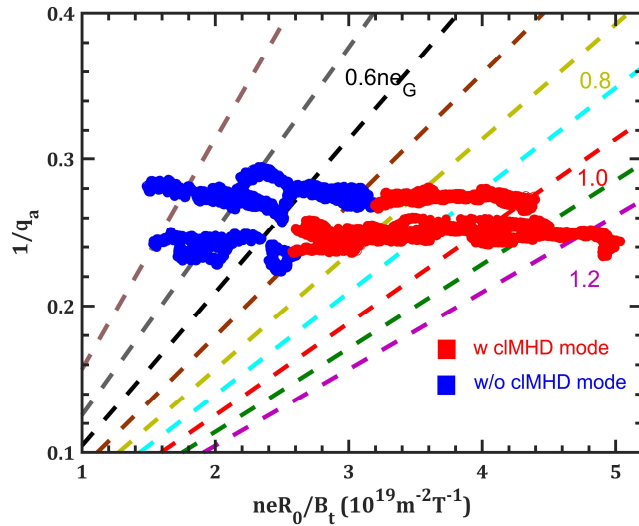


**Figure 9.** Hugill plot for high-density ohmic-heating plasmas in HL-2A. The safety factor at the plasma boundary is denoted by  $q_a$ . The dashed lines in plot indicates relationship with Greenwald density limit. Red and blue symbols represent discharges with and without clMHD modes, respectively. Here, only shots where clMHD modes occur are counted.

even though the plasma density continues to increase (as seen in Fig. 4). This decrease in SXR intensity can be attributed to a drop in electron temperature. Figure 8(a3) further shows that a rapidly growing  $m/n=-2/-1$  TM triggers a density-limit disruption. Integrating these results with those from Fig. 7, it can be inferred that the safety factor profile—or more broadly, the magnetic configuration of the plasma—significantly influences the clMHD instabilities that precede the density limit.

The physical scenario of the density limit in HL-2A ohmic-heated plasmas can be summarized as follows. Following gas puffing, the plasma density rises and the density profile becomes more peaked, accompanied by an overall decrease in electron temperature. As the density approaches the Greenwald limit, strong density gradient or  $\beta$ -induced clMHD modes develop in the plasma. These clMHD modes generally appear as density perturbations. Typically, within tens of milliseconds after the appearance of these clMHD modes, tearing modes exhibit rapid growth, leading to plasma disruption. The impact of clMHD modes on tearing modes requires further investigation, such as their effects on transport and current density profiles.

Figure 9 shows the Hugill plot [35] for high-density Ohmic-heated plasmas in the HL-2A tokamak. Red symbols correspond to discharges with clMHD modes, while blue symbols represent those without such modes. A clear threshold is observed for the occurrence of these clMHD modes at approximately  $0.7neG$  in HL-2A Ohmic-heated plasmas. As shown in Figure 9, these clMHD modes occur within the range  $0.23 < 1/q_a < 0.28$ , corresponding to  $3.6 < q_a < 4.3$ . In addition, as indicated in Figure 7 and 8, these clMHD modes often arise in the absence of sawtooth oscillations, implying

that the core safety factor  $q_0$  exceeds 1 when these modes are present. At the same time, since the eventual density-limit disruption is triggered by  $m/n=2/-1$  TMs, the core safety factor  $q_0$  should be less than 2. Therefore, the safety factor profile can be estimated as follows: in the core region,  $1 < q_0 < 2$ , and at the plasma edge,  $3.6 < q_a < 4.3$ . Due to the absence of auxiliary heating, the safety factor increases slowly and monotonically from the core to the edge, resulting in weak magnetic shear  $s = (r/q)(dq/dr)$  in the plasma core. This suggests that these clMHD modes are more easily excited under conditions of weak magnetic shear and high plasma density.

## 5 Identification of clMHD modes as KBM/AITG and their impact

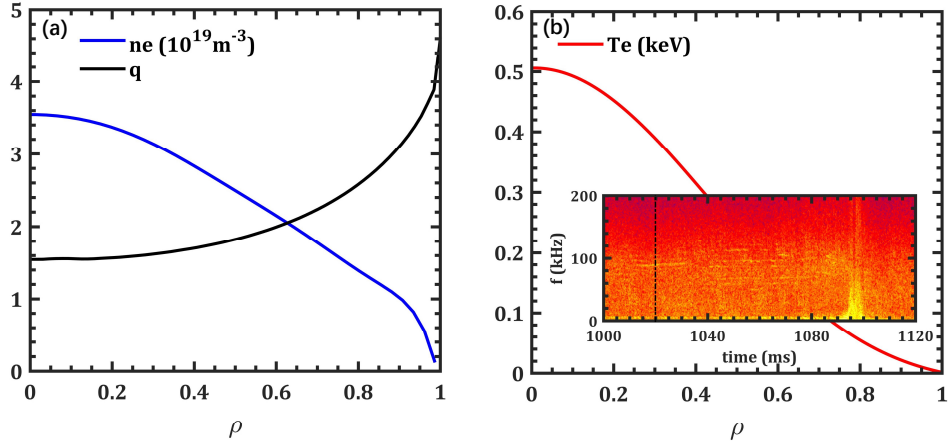


**Figure 10.** (a) Electron density  $ne$  profile and safety factor  $q$  profile for shot #38524 at 1020 ms. (b) Electron temperature  $Te$  profile provided by ECE and spectrum of microwave interferometry signal. The black dashed line indicates the time (1020 ms) at which the profiles are shown. The instability frequency at this time is approximately 90 kHz.

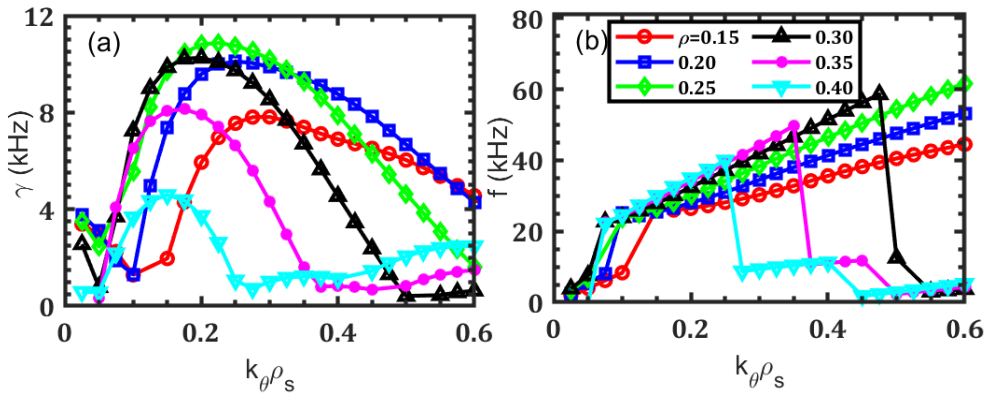


**Figure 11.** Linear GENE simulation results for the KBM instability using experimental profiles from shot #38524 at 1020 ms. (a) Growth rate  $\gamma$  (b) real frequency  $f$  are plotted against the normalized poloidal wavenumber  $k_\theta \rho_s$ , where  $\rho_s$  is the ion sound gyroradius. Each color represents a different normalized radius  $\rho = r/a$ .

To identify the core instabilities in high-density plasmas, numerical simulations were carried out using experimental parameters from a representative discharge. Figure 10 shows the radial profiles of electron density  $ne$  and electron temperature  $Te$  and safety factor  $q$  at 1020 ms for shot #38524. Given that it is an ohmic heating plasma and ion temperature data is lacking, it is assumed in the simulation that the ion temperature equals the electron temperature. Through estimation, at the moment depicted in Figure 10, the energy exchange time between electrons and ions in the plasma,  $\tau_{ei}$ , is on the order of milliseconds, which is much shorter than the energy confinement time  $\tau_E$ . Therefore, it can be assumed that the ion temperature is roughly equal to the electron temperature. The spectrum of the microwave interferometry signal for shot #38524 is also depicted in Figure 10(b). It is noteworthy that in Figure 10(a), the black solid line represents the safety factor profile. As evident, the safety factor profile for shot #38524 precisely matches the previously described safety factor profile. At 1020 ms, an instability is observed near 90 kHz. These profile data were used as

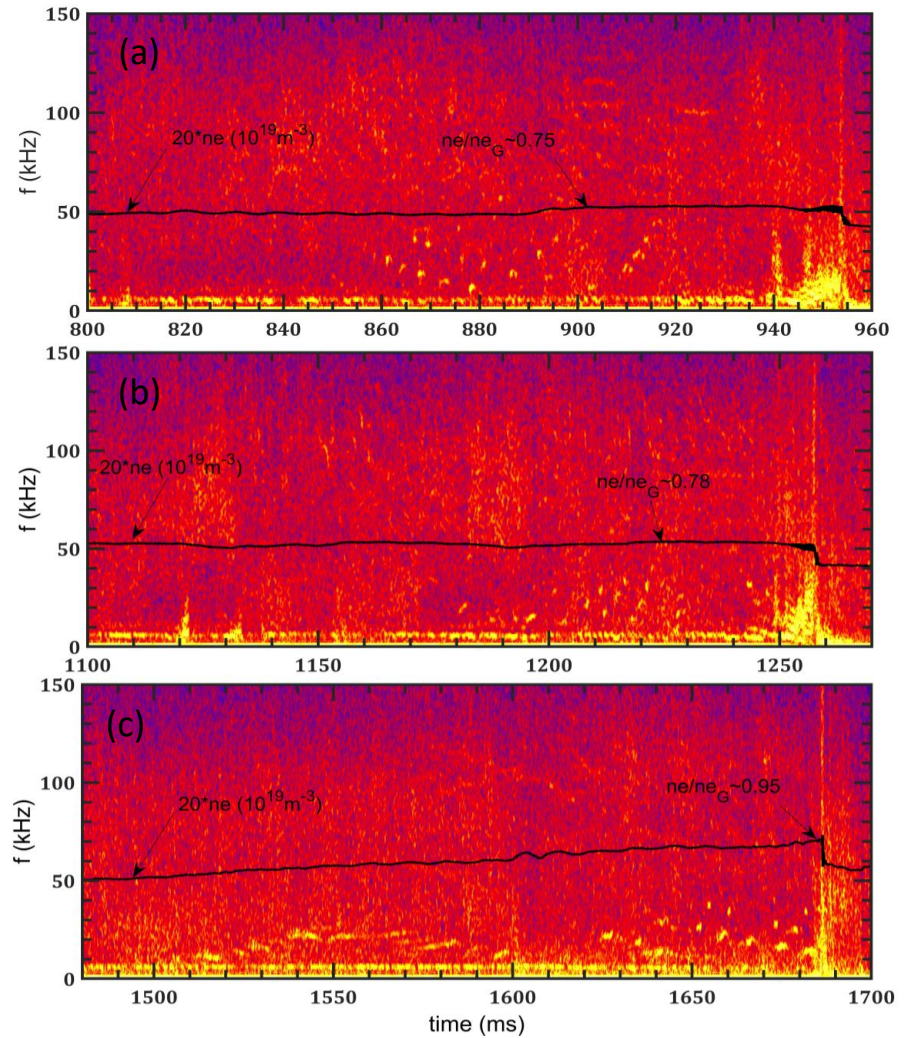


**Figure 12.** Microwave interferometry spectra are shown for three discharges: (a) #38635, (b) #38638, and (c) #38273. The black line in each panel represents 20 times of electron density  $20 * ne$  and the unit is  $10^{19} \text{ m}^{-3}$ . Black arrows point to the times when "Christmas-light" modes emerge in the spectrum.

input to the GENE code [36] to compute linear stability. Figure 11 shows the result of growth rate  $\gamma$  and real frequency  $f$  as functions of normalized poloidal wavenumber  $k_\theta \rho_s$ . And the different color lines in Figure 11 indicate different normalized radius  $\rho$ . Under the parameter conditions shown in Figure 10, it is estimated that the ion diamagnetic drift frequency  $f_{*pi}$  and the ion transit frequency  $f_{ti}$  are approximately 20 kHz. Therefore, it can be concluded from the frequency characteristics that the dominant modes in Figure 11 are the KBM/AITGs. The simulations show that KBM/AITG is unstable under the conditions of shot #38524 at 1020 ms. As seen in Figure 11(a), KBM/AITG modes are unstable over a broad radial range, e.g.,  $0.15 < \rho < 0.4$ . The peak growth rate occurs at  $k_\theta \rho_s \sim 0.25$  for  $\rho = 0.25$ , with a corresponding real frequency of about 32 kHz. The frequency difference between the instabilities in Figure 10 and Figure 11 can be attributed to Doppler shift. Due to the lack of effective diagnostic data for the toroidal rotation frequency in Ohmic-heated plasma, a direct comparison between the experimental and simulated mode frequencies could not be established. The eigenmode structure obtained from GENE simulations exhibits only slight frequency variation across radius, consistent with the spectral behavior observed in Figure 10.

Through GENE simulations, the cIMHD modes observed in high-density Ohmic-heated HL-2A plasmas have been identified as KBM/AITG-type modes. Next, we will discuss the impact of KBM/AITG modes on the plasma. Figure 12 presents additional examples of high-density ohmic discharges in which only low-frequency instabilities ( $< 50$  kHz) appear in the microwave interferometry spectra. As shown in panels (a)–(c), these low-frequency modes emerge once the Greenwald fraction  $ne/ne_G$  reaches certain thresholds—ranging from 0.75 to 0.95—and generally precede density-limit disruptions. These modes closely resemble the "Christmas-light" modes reported on DIII-D [37].

The frequency variations among instabilities result from differences in the toroidal mode number

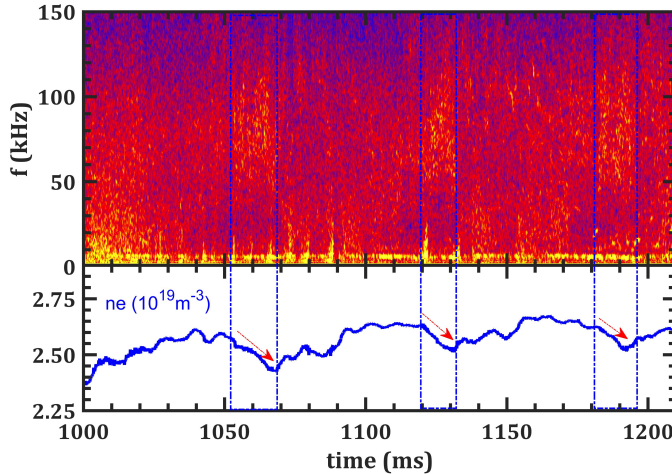


**Figure 13.** Microwave interferometry spectrum and the corresponding line-averaged density trace (blue) for shot #38638. Blue dashed lines mark the time interval during which core-localized modes appear. Red arrows indicate the trend in line-averaged density following the onset of these modes.

*n*. As evidenced by DIII-D results, the mode frequencies in the plasma frame remain nearly constant. According to the relation  $f_{lab} = f_{plasma} + n f_{v\phi}$ , the frequency shifts seen in Figure 12 are due to a decrease in *n*. A key question is what causes this decrease in toroidal mode number. In DIII-D experiments, such variations are linked to changes in the minimum safety factor  $q_{min}$ . Based on the experimental data from DIII-D, the variation in the toroidal mode number *n* originates from changes in the minimum safety factor  $q_{min}$ . However, in the high-density ohmic heating plasmas studied here, reversed magnetic shear seldom occurs, so  $q_{min}$  remains at the plasma center. This results in a weak magnetic shear configuration in the core region, as illustrated in Fig. 10(a). Therefore, the change in *n* must originate from local variations in the safety factor profile  $q(r)$  at the mode location.

The difference in toroidal mode number between two adjacent modes is 1, so the frequency spacing between them equals the toroidal rotation frequency. Taking Fig. 12(c) as an example, modes appear as bright spots in the spectrum. Those that align along a straight line are considered a group; the frequency spacing between adjacent modes in the same group is about 3.3 kHz, implying a local toroidal rotation frequency of the same value. The last mode in this group appears at approximately 15.6 kHz, and within 5 ms after its emergence, a minor density-limit disruption occurs. Since the plasma-frame frequency  $f_{plasma} > 0$ , the toroidal mode number for this mode must satisfy  $n < 5$ .

The radial width of an Alfvénic instability in a region of weak magnetic shear can be estimated as  $\Delta_m \sim r_m/(n^{1/2} S q_m)$ [38], where  $r_m$  is the minor radius at the location of the mode, *n* is the toroidal mode number of the mode,  $S = \sqrt{r_m^2 q_m''/q_m^2}$  is the generalized shear value, and  $q_m$  is the safety factor at the location of the mode. Assuming that  $r_m$ ,  $q_m$  and *S* do not change significantly over short timescales, a decrease in *n* leads to an increase in the mode's radial width. This broadening appears linked to the onset of density-limit disruptions, as shown in Figure 12(a)–(c): disruptions tend to occur after *n* has decreased sufficiently—that is, after the modes have radially expanded. A plausible explanation is that these cLMD instabilities degrade particle or energy confinement, and their effect strengthens as their radial width increases, eventually triggering a disruption. Their role in particle transport will be examined in detail later.

The high-frequency instabilities ( $\sim 100$  kHz) shown in Figure 5(a) exhibit dynamics similar to those of low-frequency KBM/AITG modes. Their frequencies satisfy  $f \sim f_{TAE} > f_{ti}$ , where  $f_{ti} = v_{\parallel}/(2\pi q R)$  represents the transit frequency of passing ions. It is expected that finite compressibility of the core plasma will significantly influence mode dynamics via resonant interaction with ion transit motion along magnetic field lines [39]. Since the fraction of trapped particles in a tokamak scales as  $f_{trap} = (2r_{\perp})^{1/2}$ , the majority of particles in the core region are passing particles. The transit frequency of thermal ions resonates with KBM dynamics, leading to  $f_{KBM} \sim f_{ti}$ . High-frequency instabilities in the core may similarly interact with thermal passing ions. The difference in frequencies between high- and low-frequency modes may result from different toroidal mode numbers and different mode location, producing discrete features in the frequency spectrum.

The experimental data presented in Figure 13 provide evidence of the role played by KBM/AITG modes in electron transport on the HL-2A tokamak. The figure displays the microwave interferometry spectrum alongside the line-averaged density for shot #38638, with blue dashed lines highlighting intervals of KBM/AITG activity. A clear reduction in plasma density is observed following the emer-

gence of these modes, which is likely due to enhanced particle transport in the core region induced by the KBM/AITGs. Consequently, these instabilities are implicated in limiting the achievable plasma beta, as they lead to a reduction in both electron temperature and density.

## 6 Summary

In Ohmic-heated plasmas in the HL-2A tokamak, the Greenwald density limit was exceeded by means of gas puffing, achieving a maximum density fraction of  $ne/ne_G \sim 1.5$  for a duration of nearly 500 ms, or about  $30\tau_E$ . Some clMHD modes are observed prior to both major and minor disruptions and are considered to contribute to their onset. Comparative analysis of soft X-ray signals, magnetic probe signals, and density profiles indicated that these clMHD modes are easier to be unstable when central safety factor is larger than 1. The clMHD modes identified in spectra are found to limit the achievable plasma density. In microwave interferometry spectra, broadband perturbations are also observed as plasma density rises. Spectral broadening increases with rising plasma density, with the maximum perturbation frequency reaching about 200 kHz before a density-limit disruption occurs.

The clMHD modes have been identified as KBM/AITG type through simulations with the GENE code. Statistical analysis of experimental data further shows that their excitation correlates with a threshold in the Greenwald density fraction, approximately  $ne/ne_G \sim 0.7$  in HL-2A Ohmic-heated plasmas. It is also observed that the toroidal mode number of these KBM/AITGs decreases with increasing density, corresponding to a broadening of the modes' radial width. Experimentally, KBMs/AITGs have been shown to directly reduce the line-averaged plasma density, indicating that they can enhance particle transport. Consequently, KBM/AITGs play a critical role in limiting the plasma density in high-density Ohmic discharges. These results provide important insight into the mechanisms underlying the density limit.

## Acknowledgments

One of the authors (W. Chen) is very grateful to the HL-2A group. This work is supported in part by NSFC under Grants No. 12125502, 12375211, 12475215 and 12205034, by the National MCF Energy R&D Program under Grants No. 2024YFE03190004, by SWIP innovation under Grants No. 202301XWCX001, and by the Nature Science Foundation of Sichuan Province under Grants No.2025ZNSFSC0833 and 2025ZNSFSC0059.

## References

- [1] Greenwald. M. *et al.* A new look at density limits in tokamaks. *Nuclear Fusion*, 28(12):2199–2207, 1988.
- [2] Greenwald. M. Density limits in toroidal plasmas. *Plasma Physics and Controlled Fusion*, 44(8):R27–R53, 2002.
- [3] Kirneva. N.A. *et al.* High density experiments in TCV ohmically heated and L-mode plasmas. *Plasma Physics and Controlled Fusion*, 57:025002, 2015.
- [4] Rapp. J. *et al.* Density limits in TEXTOR-94 auxiliary heated discharges. *Nuclear Fusion*, 39(6):765–776, 1999.
- [5] Pucella. G. *et al.* Density limit experiments on FTU. *Nuclear Fusion*, 53(8):083002, 2013.
- [6] White. R. B. *et al.* Thermal island destabilization and the Greenwald limit. *Physics of Plasmas*, 22(2):022514, 2015.
- [7] Teng. Q. *et al.* A predictive model for the tokamak density limit. *Nuclear Fusion*, 56(10):106001, 2016.
- [8] Long. T. *et al.* Enhanced particle transport events approaching the density limit of the j-text tokamak. *Nuclear Fusion*, 61(12):126066, 2021.
- [9] Long. T. *et al.* The role of shear flow collapse and enhanced turbulence spreading in edge cooling approaching the density limit. *Nuclear Fusion*, 64(6):066011, 2024.
- [10] Giacomin. M. *et al.* Investigation of turbulent transport regimes in the tokamak edge by using two-fluid simulations. *Journal of Plasma Physics*, 86(5):905860502, 2020.
- [11] Giacomin. M. *et al.* Turbulent transport regimes in the tokamak boundary and operational limits. *Physics of Plasmas*, 29(6):062303, 2022.

- [12] Lang. P.T. et al. High-density H-mode operation by pellet injection and ELM mitigation with the new active in-vessel saddle coils in ASDEX Upgrade. *Nuclear Fusion*, 52(2):023017, 2012.
- [13] Bell. M. G. et al. Attainment of high plasma densities in TFTR with injection of multiple deuterium pellets. *Nuclear Fusion*, 32(9):1585–1591, 1992.
- [14] Gates. D. A. et al. Origin of tokamak density limit scalings. *Physical Review Letters*, 108(16):165004, 2012.
- [15] Rice. J.E. et al. Understanding LOC/SOC phenomenology in tokamaks. *Nuclear Fusion*, 60(10):105001, 2020.
- [16] Chen.W. et al. Alfvénic ion temperature gradient activities in a weak magnetic shear plasma. *Europhysics Letters*, 116(4):45003, 2016.
- [17] Connor. J. W. et al. Shear, periodicity, and plasma ballooning modes. *Physical Review Letters*, 40(6):396–399, 1978.
- [18] Belli. E. A. et al. Fully electromagnetic gyrokinetic eigenmode analysis of high-beta shaped plasmas. *Physics of Plasmas*, 17(11):112314, 2010.
- [19] Kumar. N. et al. Turbulent transport driven by kinetic ballooning modes in the inner core of JET hybrid H-modes. *Nuclear Fusion*, 61(3):036005, 2021.
- [20] Xu. J. Q. et al. Gyrokinetic analysis of turbulent transport by electromagnetic turbulence in finite plasmas with weak magnetic shear on HL-2A. *Nuclear Fusion*, 63(12):126031, 2023.
- [21] Drake. J.F. et al. Kinetic theory of tearing instabilities. *The Physics of Fluids*, 20(8):1341–1353, 1977.
- [22] Duan. X. R. et al. Overview of experimental results on HL-2A. *Nuclear fusion*, 49(10):104012, 2009.
- [23] Li. Y. G. et al. A new high sensitivity far-infrared laser interferometer for the HL-2A tokamak. *Review of Scientific Instruments*, 88(8), 2017.
- [24] Shi. P. W. et al. Multichannel microwave interferometer for simultaneous measurement of electron density and its fluctuation on HL-2A tokamak. *Plasma Science and Technology*, 18(7):708–713, 2016.
- [25] Shi. Z. B. et al. Calibration of a 32 channel electron cyclotron emission radiometer on the HL-2A tokamak. *Review of Scientific Instruments*, 85(2), 2014.
- [26] X. Q. Ji . et al. Identification and analysis of magnetic structures on hl-2a. *Plasma Science and Technology*, 8(6):644–648, 2006.
- [27] Nazikian. R. et al. Toroidal alfvén eigenmodes in TFTR deuterium–tritium plasmas. *Physics of Plasmas*, 5(5):1703–1711, 1998.
- [28] Strait. E. J. et al. Doppler shift of the tae mode frequency in DIII-D. *Plasma physics and controlled fusion*, 36(7):1211, 1994.
- [29] Freidberg. J. P. *Plasma physics and fusion energy*. Cambridge university press, 2008.
- [30] Chen. W. et al. Core-localized Alfvénic modes driven by energetic ions in HL-2A NBI plasmas with weak magnetic shears. *Nuclear Fusion*, 56(3):036018, 2016.
- [31] Chen. W. et al. Kinetic electromagnetic instabilities in an ITB plasma with weak magnetic shear. *Nuclear Fusion*, 58(5):056004, 2018.
- [32] Zonca. F. et al. Kinetic theory of low-frequency Alfvén modes in tokamaks. *Plasma Physics and Controlled Fusion*, 38(11):2011–2028, 1996.
- [33] Ma. R. R. et al. Low-frequency shear Alfvén waves at DIII-D: Theoretical interpretation of experimental observations. *Physics of Plasmas*, 30(4), 2023.
- [34] Hou. Y. W. et al. NIMROD calculations of energetic particle driven toroidal Alfvén eigenmodes. *Physics of Plasmas*, 25(1):012501, 2018.

- [35] Stabler. A. et al. Density limit investigations on ASDEX. *Nuclear Fusion*, 32(9):1557–1583, 1992.
- [36] Jenko. F. et al. Electron temperature gradient driven turbulence. *Physics of Plasmas*, 7(5):1904–1910, 2000.
- [37] Heidbrink. W.W. et al. ‘BAAE’ instabilities observed without fast ion drive. *Nuclear Fusion*, 61(1):016029, 2021.
- [38] Zonca. F. et al. Energetic particle mode stability in tokamaks with hollow q -profiles. *Physics of Plasmas*, 9(12):4939–4956, 2002.
- [39] Zonca. F. et al. Existence of discrete modes in an unstable shear Alfvén continuous spectrum. *Plasma Physics and Controlled Fusion*, 40(12):2009–2021, 1998.